RSC Advances

ROYAL SOCIETY OF CHEMISTRY

www.rsc.org/advances

Facile ion-exchange synthesis of urchin-shaped CdS/Bi_2S_3 heterostructures with enhanced photostability and visible light photocatalytic activity

Yunhui Yan[a,b], Zhaoxian Zhou[c]，Wuqi Li[a]，Yanjie Zhu[a], Yun Cheng[a], Fengying Zhao[a] and Jianguo Zhou[a*]

a School of Environment, Henan Normal University, Xinxiang, Henan 453007, PR China

b Department of Chemistry, Xinxiang Medical University, Xinxiang, Henan 453003, PR China

c School of Chemistry and Materials Science, University of Science and Technology of China, Hefei 230026, China

Abstract: Blackberry-like CdS microspheres were synthesized by a facile hydrothermal method. Subsequently, through a simple ion-exchange reaction between the CdS microsphere and $Bi(NO_3)_3$•$5H_2O$, novel urchin-shaped CdS/Bi_2S_3 core/shell heterostructures have successfully been fabricated. The photocatalytic activity and photostability were evaluated by degradation of rhodamine B (RhB) under visible light irradiation. The results show that the content of Bi_2S_3 had important effects on the photocatalytic activity, and the CdS/Bi_2S_3 heterostructures with the theoretical molar rate of Bi/Cd (0.25) exhibited the best photocatalytic activity. The improved photocatalytic activity and photostability were attributed to the visible light absorption enhanced by Bi_2S_3 and the formation of a heterojunction between CdS and Bi_2S_3, which can effectively accelerate the charge separation and transfer corrosive holes from CdS to robust Bi_2S_3. Experimentally and theoretically, Bi_2S_3 anchored on CdS acts as a corrosion protection agent for CdS and also acts as a co-catalyst.

Keywords: ion-exchange, cadmium sulfide, bismuth sulfide, heterostructure, photocatalyst, photocorrosion.

1. Introduction

Heterogeneous photocatalysis, an ideal "green" technology, have aroused tremendous interest for their potential applications in environmental remediation and solar conversion[1-2]. An eco-friendly efficient photocatalyst should possess a good separation of the photogenerated carriers, a wide spectral response range to maximally utilize sunlight energy, and suitable band potentials to produce free radicals[3]. To date, most of these investigations have focused on titania (TiO_2) because of its peculiarities of chemical inertness, resistance to photocorrosion, low cost, and nontoxicity. Unfortunately, TiO_2 works only with ultraviolet (UV) radiation that does not meet the needs of solar-driven applications. In spite of extensive efforts to dope TiO_2 with metallic and nonmetallic elements, its photocatalytic activity under visible light illumination has remained quite low[4]. Therefore, it remains a major challenge to develop an excellent photocatalyst that can sufficiently harvest sunlight and effectively promote charge separation.

Compare to metal oxides, some of metal sulfides are promising visible-light-driven photocatalysts because of their desired band-gap width and suitable band-edge positions[5-6]. Among them, Cadmium sulfide (CdS) is a fascinating material with band gap of ~2.4 eV, which make it become a good candidate for the splitting of water or degradation of organic pollutants[7-8]. Nevertheless, before CdS can become ideal candidate for practical applications, there are two major obstacles to be tackled. First, the

photocatalytic efficiency of CdS is severely restricted by the fast recombination of photoexcited charge carriers[9]. Even worse, CdS alone is prone to photocorrosion in aqueous solution via self-oxidation by photogenerated holes during the photocatalytic reaction[10-13]. Therefore, an enormous amount of effort has been devoted to either reducing the recombination of photogenerated carriers or suppressing the photocorrosion of CdS[13-14]. For instance, coupling CdS with another semiconductor (TiO_2, SnO_2, etc.) or noble metal could generate an interface electric field by band-edge offset, which can effectively accelerate the separation and transfer of photogenerated carriers[15-16]. Then, how to solve the photocorrosion problem? Apparently, the effectively taking photogenerated holes away from the valence band of CdS would improve its stability effectively. The use of Na_2S and Na_2SO_3 as electron donor for CdS in photocatalytic reaction system has been considered as one of the important methods to improve the stability of CdS[17-18]. Additionally, CdS can also be protected by being coated with or encapsulated into amorphous carbon or polymeric materials, such as conducting polyaniline (PANI)[19] and polymeric carbon nitride material (C_3N_4)[20-21].

Bismuth sulfide (Bi_2S_3) is a significant lamellar structured semiconductor with a narrow bandgap of ~1.3 eV, which has been used in the fields of electrochemical hydrogen storage, photovoltaics and thermoelectrics, and so on[22-23]. The narrow band gap and large absorption coefficient make it become an ideal candidate for photoresponsive materials[24-25]. Bi_2S_3 nanoparticles with different sizes and Fe_3O_4-Bi_2S_3 core-shell

hierarchical structures showed high efficiency in photodegradation of RhB [22, 26]. More recently, Bi_2S_3 has been acted as a sensitizer due to its ability to absorb a large part of visible light up to 800 nm[27]. The combination of CdS and Bi_2S_3 by the means of forming heterojunction might be an efficient way for the separation of photoinduced carries, and thus raise photocatalytic efficiency of the composites. For instance, A. Jana et al.[28] and Mishra et al.[29] have synthesized the CdS-Bi_2S_3 composites by an electrochemical method, respectively. The results showed that the as-prepared composites exhibited substantial improvement of photoelectrochemical activity. X. Li et al.[30] prepared the Bi_2S_3/CdS photocatalysts by direct precipitation method and investigated their photocatalytic activities for reducing CO_2 to CH_3OH. Z. Fang et al.[31] has obtained the Bi_2S_3/CdS heterostructure through sequential deposition growth processes. The results indicated that the heterostructures exhibited enhanced photochemical efficiency for the degradation of methyl red (MR) under UV irradiation. However, the photocatalytic activity and photostability of the CdS/Bi_2S_3 heterostructures under visible light radiation has not yet been reported.

Herein, we demonstrate a facile ion-exchange method for anchoring Bi_2S_3 nanorods onto CdS microspheres to construct core/shell CdS/Bi_2S_3 heterostructure, with first-time usage of these novel heterostructures for the degradation of organic dyes under visible light radiation. The as-prepared CdS/Bi_2S_3 heterostructure exhibits enhanced photocatalytic efficiency and stability compared with pure CdS, which could be attributed

not only to the enhancement of light-harvesting capacity by Bi_2S_3 but also to the effective separation of photogenerated carriers driven by the electrostatic field in the CdS/Bi_2S_3 junction.

2. Experimental

2.1. Synthesis of CdS microspheres

All the chemicals were analytical grade reagents and used as received without further purification. Deionized water was used throughout this study.

In a typical synthesis, 2 mmol $Cd(CH_3COO)_2•2H_2O$ and 4 mmol $CS(NH_2)_2$ were dissolved in 30 mL deionized water. After stirring for 30 min, the mixture was transferred into a 50 mL Teflon-lined stainless-steel autoclave, heated to 150 °C and maintained for 2 h. After the autoclave was cooled to room temperature, the products were separated centrifugally and washed with deionized water and absolute ethanol for several times, and then dried under vacuum at 60 °C for 8 h.

2.2. Synthesis of CdS/Bi_2S_3 heterostructures

The CdS/Bi_2S_3 heterostructures were synthesized via a simple ion-exchange reaction between CdS microspheres and $Bi(NO_3)_3•5H_2O$. In a typical process, the as-prepared CdS microsphere (0.1445 g, 1 mmol) was dispersed to 25 mL ethylene glycol (EG) under ultrasonication. After 30 min, 0.0485 g, 0.1 mmol $Bi(NO_3)_3$/EG solution (25 mL) was added dropwise into the above suspension liquid at room temperature. The whole mixture was maintained at 80 °C for 1 h with magnetic stirring. The products were collected by

centrifugation, washed with deionized water and absolute ethanol for several times. Finally the obtained samples were dried in vacuum at 60 °C for 8 h. By changing the amount of the added Bi^{3+} ion, a series of CdS/Bi_2S_3 heterostructures were prepared. The theoretical molar rates of the added Bi to initial Cd were 0.1, 0.25, 0.5, and 1, and the resulting samples were labeled as BC-0.1, BC-0.25, BC-0.5 and BC-1.0, respectively.

For comparison, pure Bi_2S_3 was prepared as follows: 0.4851 g (1.0 mmol) of $Bi(NO_3)_3 \cdot 5H_2O$ was dissolved in 30 mL ethylene glycol (EG) to form a clear solution. Subsequently, 4 mmol of $CS(NH_2)_2$ was added into this solution. After stirring for 30 min, the mixture was transferred into a 50 mL Teflon-lined stainless-steel autoclave. The autoclave was heated to 150 °C and maintained for 8 h, and then cooled to room temperature. The product was separated and washed, and dried in vacuum at 60 °C for 8 h.

2.2. Characterization

The crystal structures of the obtained samples were performed on a Bruker D8 Advance X-ray diffractometer using Cu Kα radiation (λ=0.15418 nm). The XPS data were taken on an AXIS-Ultra instrument from Kratos Analytical using monochromatic Al Ka radiation (1486.71 eV). The morphology of the as-prepared samples was examined by transmission electron microscopy (TEM, JEM-2100) and scanning electron micrography (SEM, JSM-6390LV). UV-vis diffuse reflectance spectra (DRS) were recorded on a Lambda 950 Spectrophotometer (Perkin Elmer) using $BaSO_4$ as reference. The photoluminescence (PL) spectra of photocatalysts were recorded using a Fluorescence Spectrophotometer (FP-6500, Janpan) at room temperature with an excitation wavelength

of 365 nm.

2.3. Photocatalytic activity and photocorrosion test

The photocatalytic activities of the as-prepared samples were evaluated by degradation of rhodamine B (RhB) under visible light radiation from a 500 W Xe lamp equipped with a 420 nm cutoff filter. In each experiment, 50 mg catalyst was added into 100 mL RhB solution (10 mg/L). Before illumination, the suspensions were magnetically stirred in the dark for an hour to ensure the establishment of an adsorption-desorption equilibrium between the photocatalysts and RhB. The suspension was under constant vigorous stirring with the photoreactor during the process and the temperature of the suspension was maintained at 25 °C by circulation of water. At given time intervals of illumination, 5 mL suspensions were sampled and centrifuged to remove the photocatalyst powders for further analysis.

The concentration of RhB was determined by measuring the absorption intensity at its maximum absorbance wavelength (553 nm) using a UV-vis spectrophotometer (UV-2450). The degradation efficiency of RhB was calculated by the following equation:

$$\text{Degradation rate} = (C_0 - C)/ C_0 \times 100\% = (A_0 - A)/ A_0 \times 100\% \quad (1)$$

Here, C is the solution concentration of RhB, C_0 is the initial concentration, A is the absorbance of RhB solution after degradation, and A_0 is the initial absorbance of RhB solution before degradation.

In order to determine photostability of the catalyst, the cycle experiments were carried out. The target catalyst and clear supernatant liquid were separated and collected by high speed centrifugation. After being washed with water for 3 times and dried in vacuum at 60 °C for 8 h, the catalyst was reused with a fresh RhB aqueous solution for subsequent reactions under the same conditions. The concentration of released Cd^{2+} in the reaction solution was determined by inductively coupled plasma mass spectrometry (ICP-MS, Perkin Elmer SCIEX ElAN DRC-e). The separated catalysts were also characterized by XRD.

3. Results and discussion

3.1 Phase structure and chemical composition

Bi_2S_3 is a product with a rather lower solubility ($Ksp=1\times10^{-97}$), and thus CdS can transform to Bi_2S_3 with the presence of Bi^{3+} ions, and the CdS/Bi_2S_3 heterostructure can be easily formed on CdS. The reaction between Bi^{3+} ions and CdS can be described as[32]:

$$3CdS + 2Bi^{3+} \rightarrow Bi_2S_3 + 3Cd^{2+} \quad (2)$$

Actually, the dissolution of the CdS mother is not visible without introducing Bi^{3+} ions. The existence of Bi^{3+} ions can accelerate the dissolution of CdS.

In order to successfully provide Bi^{3+} ions, ethylene glycol (EG) was selected as the solvent. The first reason is that $Bi(NO_3)_3\bullet5H_2O$ is easily hydrolyzed in aqueous solution, while it can be successfully dissolved in the solvent EG to form Bi^{3+} ions. On the other hand, due to smaller polarity and larger viscosity, EG can alleviate the reaction rate of the ion exchange above and facilitate the formation of intimate interfaces.

The crystal structure and phase composition of the as-obtained samples were investigated by XRD measurements. Fig.1 shows the XRD patterns of the CdS/Bi_2S_3 heterostructures, as well as the pure CdS and Bi_2S_3 samples. As can be seen from Fig.1a and f, all of the diffraction peaks can be indexed as well-crystallized hexagonal CdS (JCPDS No. 77-2306)[33] and orthorhombic Bi_2S_3 (JCPDS No. 17-0320), respectively. The successful anchoring Bi_2S_3 on the surface of CdS microspheres could be confirmed by the XRD pattern. In addition to the diffraction peaks assigned to hexagonal CdS, the XRD pattern of the CdS/Bi_2S_3 heterostructures shows 2θ peaks at 23.62° and 31.72°, which correspond to (101) and (221) planes of orthorhombic Bi_2S_3 (Fig. 1 b-e), indicating the existence of individual components of CdS and Bi_2S_3 in the CdS/Bi_2S_3 heterostructures. Moreover, the intensity of diffraction peaks represented the orthorhombic Bi_2S_3 gradually increased with the increase of Bi_2S_3. Meanwhile, it was observed that there was no peak position change in the XRD patterns, which further confirmed that the Bi_2S_3 existed in a separated phase form rather than in the CdS lattice. All the above results suggest that the Bi_2S_3 shell could in-situ grow on the surface of CdS core. The average crystallite sizes were estimated according to Scherrer formula, and the results were listed in Table 1. The results show that CdS in CdS/Bi_2S_3 samples had similar average crystalline size to pure CdS, indicating that in-situ growth of Bi_2S_3 had the minimal effect on the CdS particles.

Insert Fig.1 near here

The phase content of a sample can be calculated from the integrated intensities of

diffraction peaks from the XRD pattern[1, 34]. The weight fraction of the Bi_2S_3 (W_B) can be calculated from the equation below:

$$W_B = \frac{I_B}{I_B + I_C K_B / K_C} \qquad (3)$$

where I_B and I_C represent the integrated intensity of the (101) peak for the orthorhombic Bi_2S_3 phase and that of the (002) peak for the hexagonal CdS phase, respectively. K_B and K_C represents the specific value of reference intensity ratio (RIR) of Bi_2S_3 and CdS, which is determined to be 2.10 and 7.76, respectively.

The calculated weight fraction of the Bi_2S_3 (W_B) (see Table 1) in the CdS/Bi_2S_3 heterostructures is lower than that of the corresponding theoretical mass percentage of Bi_2S_3 to CdS. This result clearly indicates that only a part of Bi^{3+} ion can transform into Bi_2S_3 through the cation-exchange reaction. Therefore, due to low content of Bi_2S_3 or the highly dispersed Bi_2S_3, no distinct diffraction peak of Bi_2S_3 can be observed in the BC-0.1 sample.

Table 1. The theoretical molar rate, phase content, average crystallite sizes, degradation rate, reaction rate constant (k_{app}) and correlation coefficients (R^2) of different photocatalysts.

Sample	M_{Bi}:M_{Cd}[a]	W_B (%)	Average crystallite sizes/nm		Degradation rate (%)	k_{app}/min^{-1}	R^2
			CdS	Bi_2S_3			
CdS	/	/	47,79	/	80.4	1.24×10^{-2}	0.9887
BC-0.1	0.1:1	_[b]	49.54	_[b]	90.7	1.92×10^{-2}	0.9984
BC-0.25	0.25:1	10.87	51.07	21.51	97.4	3.08×10^{-2}	0.9987

BC-0.5	0.5:1	14.27	48.94	22.07	62.0	7.55×10^{-3}	0.9943
BC-1.0	1:1	40.34	46.68	23.56	49.1	5.23×10^{-3}	0.9696
Bi_2S_3	/	/	/	49.26	30.5	3.26×10^{-3}	0.9811

[a] the theoretical molar ratios of Bi to Cd for the cation exchange procedure.

[b] The Bi_2S_3 phase content was too small to be calculated from XRD patterns.

The surface chemical compositions and valence state of the BC-0.25 sample were further analyzed by X-ray photoelectron spectra (XPS). The survey scan spectrum (Fig. 2a) clearly indicates that the product is composed of Cd, Bi and S elements (C and O signals can come from ambient contamination or adsorbed impurities). The high-resolution XPS spectrum of the Cd 3d orbital region (Fig. 2b) shows the binding energies of Cd $3d_{3/2}$ and Cd $3d_{5/2}$ peaks at 412.1 and 405.3 eV, respectively. The splitting energy of 6.8 eV between Cd $3d_{3/2}$ and Cd $3d_{5/2}$ is a typical value for Cd^{2+} in CdS[35]. As for the Bi 4f spectrum (Fig. 2c), two peaks at about 164.7 eV and 159.4 eV can be assigned to Bi $4f_{5/2}$ and Bi $4f_{7/2}$, respectively. The peak separation between the Bi $4f_{5/2}$ and Bi $4f_{7/2}$ is 5.30 eV, indicating that the valence state of bismuth in the CdS/Bi_2S_3 sample was +3. Meanwhile, the peak at 225.8 eV (Fig. 2d) can be assigned to S 2s[36]. Consequently, the XPS results indicate that the products consist of CdS and Bi_2S_3 without obvious residual impurities.

Insert Fig.2 near here

3.2 Morphology

Fig. 3 shows SEM images of the CdS/Bi_2S_3 heterostructures with different Bi_2S_3

contents, as well as the pure CdS and Bi_2S_3 samples. From Fig. 3a, the large numbers of CdS microspheres with blackberry-like morphology were observed and their sizes are in the range of 1-1.5 μm. Moreover, each blackberry-like sphere is composed of many nano-sized particles and presents relatively smooth surface. It was obvious that the introduction of Bi^{3+} ions has significant influence on the morphology and microstructure of CdS microspheres. As shown in Fig. 3b, with the addition of Bi^{3+} ions at low concentration, no obvious morphology change was found except that the surface of spheres was not as smooth as pure CdS, indicating formation of nanosized Bi_2S_3 particles on CdS. For the BC-0.25 sample, the blackberry-like morphology disappeared and Bi_2S_3 nanorods can be clearly observed (Fig. 3c). When higher concentration of Bi^{3+} ions was added, more Bi_2S_3 nanorods were deposited, resulting in a relatively rough surface, as shown in Fig. 3d and e. Fig. 3f reveals that pure Bi_2S_3 sample is composed of nanorod aggregates. The diameter of the nanorods was about 0.1μm and the length was up to 1μm.

Insert Fig.3 near here

The detailed structural information about the BC-0.25 sample was further investigated by TEM, HRTEM and EDS. The inset in Fig. 4a shows an individual TEM image of the CdS/Bi_2S_3 heterostructures, which clearly reveals that the sphere basically looked like urchin shape with diameter of *ca.* 1.2 μm. The magnified TEM image (Fig. 4a) further confirms that some Bi_2S_3 nanorods were grown on CdS microspheres. The HRTEM image recorded from the region of the sample is shown in Fig. 4b. The spacing

of the adjacent lattice fringes is about 0.352 nm, which is consistent with the (310) lattice planes of orthorhombic Bi_2S_3. The electron dispersive spectroscopy (EDS, Fig. 4c) suggests the presence of S, Cd, and Bi elements (the C and Cu signals come from the holey carbon TEM grid), further revealing that Bi_2S_3 was successfully combined with CdS.

Insert Fig.4 near here

3.3 Optical properties

The UV-vis diffuse reflectance spectra (DRS) were measured to investigate the optical absorption property of the samples. Pure CdS and Bi_2S_3 were also studied for comparison. As can be seen, the pure CdS sample (Fig. 5a) can absorb visible light with wavelengths shorter than 560 nm. Compared with pure CdS, all the CdS/Bi_2S_3 heterostructures (Fig. 5b-e) clearly show an optical response in the visible region. They all have strong absorption in the UV-visible-light range, and even in the infrared region, implying that these samples have visible-light photocatalytic activity. The content of Bi_2S_3 contributes to tune the optical properties of the CdS/Bi_2S_3 heterostructures, and their absorption band has a significant red-shift with the increase of Bi_2S_3.

For a semiconductor, the absorbance near the band edge obeys the formula: $\alpha h\nu = A(h\nu - Eg)^{n/2}$, where α is the absorption coefficient, $h\nu$ is the photon energy, A is a constant, and Eg is the band gap. The value of n depends on whether the transition is direct (n= 1) or indirect (n= 4) in a semiconductor. CdS and Bi_2S_3 are direct transition,

thus, n is equal to 1. From the plot of $(\alpha h\nu)^2$ vs $(h\nu)$ in the inset of Fig.5, the value of Eg for the pure CdS and Bi_2S_3 was estimated to be 2.20 and 1.30eV, which was consistent with literature values[37-38] . For the CdS/Bi_2S_3 heterostructures, the band gap value was 1.90, 1.85, 1.50, and 1.45 eV, corresponding to the sample BC-0.1, BC-0.25, BC-0.5 and BC-1.0, respectively. The decrease in band gap energy indicates that CdS/Bi_2S_3 heterostructures have much greater optical absorption ability than pure CdS, which can be excited to produce more electron-hole pairs under the same visible light illumination and then resulting in higher photocatalytic activity.

Insert Fig.5 near here

Since photoluminescence (PL) emission mainly arises from the recombination of free carriers, PL spectroscopy is a facile technique to survey the separation efficiency of photoinduced electron-hole pairs in a semiconductor[39]. Fig. 6 shows the room temperature photoluminescence spectra of pure CdS, Bi_2S_3 and the BC-0.25 sample with an excitation wavelength of 365 nm. The pure CdS exhibits a strong PL emission peak centered at about 575 nm, while pure Bi_2S_3 displays almost no luminescence peak in the scope of monitoring. For the BC-0.25 photocatalyst, however, the intensity of the emission peak significantly decreases, demonstrating that the separation efficiency of the photogenerated electrons and holes in the heterostructured photocatalyst is markedly improved as a result of the synergistic effect between CdS and Bi_2S_3.

Insert Fig.6 near here

3.4 Photocatalytic activity

The photocatalytic activities of the as-prepared samples were evaluated by degradation of RhB under visible light radiation. Fig. 7 shows the temporal evolution of the absorption spectra of RhB solution in the presence of pure CdS, Bi_2S_3 and the BC-0.25 samples. As can be seen from the above three spectra, the absorbance of RhB in Bi_2S_3 nanorods suspension is hardly changed. This result shows that Bi_2S_3 has lower photocatalytic activity under the experimental conditions, owing to the rapid recombination of photoinduced electrons and holes. The absorbance of RhB in both CdS and CdS/Bi_2S suspensions gradually decreased during the photodegradation process. Additionally, the slight blue-shift of the major absorption peak (553 nm) was observed for the de-ethylation of RhB, which was in agreement with the previous literature[40]. An especially remarkable decrease in absorbance of RhB was observed over the BC-0.25 sample, indicating that the CdS/Bi_2S heterostructure exhibits high photocatalytic efficiency in RhB degradation.

Insert Fig.7 near here

Fig. 8a shows the photocatalytic activities of different catalysts. It can be seen that self-degradation of RhB is negligible, indicating the stabilization of RhB molecule. The CdS/Bi_2S_3 heterostructures show higher photocatalytic activities than individual CdS and Bi_2S_3, especially the BC-0.25 sample, which exhibited the best photocatalytic activity, and the photodegradation efficiency reached 97.4% after 2 h. The high photocatalytic

activity of the CdS/Bi_2S_3 heterostructure can be attributed to the increased light absorptivity and charge separation of CdS caused by the Bi_2S_3 nanorods. However, when excess Bi_2S_3 was introduced, the surface of CdS were almost completely coated with Bi_2S_3 and the active sites for the degradation of organic dyes via CdS were reduced, meanwhile, excess Bi_2S_3 can become a recombination center for photogenerated electrons and holes, leading to photoactivity fading.

Insert Fig.8 near here

The kinetics of the degradation reaction can be described using a first-order model for low concentrations of RhB solutions. The pseudo first-order kinetics equation is expressed as $\ln(C_0/C) = k_{app}t$, where C and C_0 are the concentration and initial concentration of RhB, respectively, t is the irradiation time and k_{app} denotes the apparent reaction rate constant [1, 41]. The relation between $\ln(C_0/C)$ and irradiation time (t) is plotted in Fig. 8b. The values of k and the corresponding correlation coefficients R^2 were calculated and listed in Table 1. The excellent fitness indicates that the photoreaction follows the way of first-order reaction kinetics. From Table 1, it was found that the degradation rate constant of BC-0.25 was about 2.5 and 9.5 times higher than those of pure CdS and Bi_2S_3, respectively.

3.5 Photostability

The capability for reuse is one of the most critical factors for an ideal photocatalyst. Hence, the reusability and stability of the BC-0.25 sample and pure CdS were investigated. The samples were collected after degradation experiments and reused three

times. As shown in Fig. 9, the pure CdS sample exhibit gradually reduced activities and only 65% of RhB can be removed in the third cycles. In contrast, only a slight drop of the efficiency is observed for the CdS/Bi_2S_3 heterostructure. This result demonstrates that the combination of CdS with Bi_2S_3 to form heterojunction can improve the stability effectively.

Insert Fig.9 near here

In order to further verify the photostability of the CdS/Bi_2S_3 photocatalysts, XRD patterns of BC-0.25 and pure CdS before and after the photocatalytic degradation for three cycles were analyzed, and the results are compared in Fig.10. For CdS, the crystallinity was destroyed seriously after photocatalytic reaction due to the photocorrosion. While for the CdS/Bi_2S_3 heterostructure, no noticeable difference was detected in the XRD patterns before and after the photocatalytic reaction. More importantly, the concentration of released Cd^{2+} in solution after the third recycle were 22.1 and 5.7 ppm, for pure CdS and BC-0.25 sample, respectively, demonstrating that the CdS/Bi_2S_3 photocatalysts possess good photostability and Bi_2S_3 has the additional function of inhibiting the leaching of CdS. The following reasons may be responsible for the results. First, coating Bi_2S_3 on the surface of CdS could reduce the areas exposed to the reaction solutions. Second, the holes transfer from the valance band of CdS to that of Bi_2S_3, which reduces CdS corrosion.

Insert Fig.10 near here

3.6 Mechanism of enhanced photoactivity and photostability

To cast light on the effect of the heterostructure on photocatalytic activity, the energy band structure was studied. The band positions of CdS and Bi_2S_3 can be predicted using the following empirical formula (4) and (5), respectively[42-43].

$$E_{VB} = \chi - E^e + 0.5E_g \quad (4)$$

$$E_{CB} = E_{VB} - Eg \quad (5)$$

where E_{VB} and E_{CB} is the valence band (VB) and conduction band (CB) edge potential, respectively; E_g is the band gap energy of the semiconductor; E^e is the energy of free electrons on the hydrogen scale (4.5 eV), and χ is the electronegativity of the semiconductor, which is the geometric mean of the electronegativity of the constituent atoms. The χ values for CdS and Bi_2S_3 are ca. 5.04 [5] and 5.27 eV[36], and the band gap energies of CdS and Bi_2S_3 are 2.20 and 1.30 eV, respectively. Given the equation above, the conduction band bottom (E_{CB}) of CdS and Bi_2S_3 is calculated to be −0.56 and 0.12 eV, respectively. Correspondingly, the tops of the valence bands (E_{VB}) of CdS and Bi_2S_3 are 1.64 and 1.42 eV, respectively.

Based on the above data, the band gap structure of the CdS/Bi_2S_3 heterostructures can be demonstrated in Fig.11. Bi_2S_3 with a narrow band gap energy (1.30 eV) could be easily excited by visible light (λ > 420 nm, energy less than 2.95 eV) and generate photoelectrons and holes. Meanwhile, electrons in the VB of Bi_2S_3 could be excited up to a higher potential edge (−1.53 eV) due to the higher photon energy[44-45]. For CdS, electrons in the VB could also be excited up to a higher potential edge (−1.31 eV) in the

same way. Therefore, the reformed CB edge potential of Bi_2S_3 (−1.53 eV) is more negative than that of CdS (−1.31 eV), photoinduced electrons on the Bi_2S_3 surface would easily transfer to CdS. Conversely, the VB edge potential of CdS is positive than that of Bi_2S_3, the photogenerated holes on CdS can rapidly migrate to the coated Bi_2S_3. In this case, an effective charge separation can be achieved, resulting in enhancement of photocatalytic activity

Insert Fig.11 near here

It is well known that CdS is not stable enough during the photocatalytic reaction because photocorrosion is prone to occur. If the photogenerated holes on CdS valence band do not transfer quickly to leave away and react with chemisorbed water and/or the adsorbed organic compounds, corrosion occurs, which will induce a release of cadmium ion in solution and the formation of an elemental sulfur layer on the surface of the CdS particles (eq 6)[13].

$$CdS + h^+ \rightarrow Cd^{2+} + S \qquad (6)$$

This may not only affect significantly the photocatalysis reaction but also cause additional environmental damage. Fortunately, as discussed above, charge transfer is directional under the heterojunction effect and the inverse motions are thermodynamically unallowed. The hole transfer is favorable from CdS to Bi_2S_3, thus Bi_2S_3 acts as a sacrificial agent by transferring the CdS corrosion to itself and maintains the continuous activity of CdS[46]. On the other hand, the existence of Bi_2S_3 on the CdS

surface can not only play the role of physical protection, but also act as a co-catalyst and provide highly active sites for the degradation of organic dyes[47-48].

4. Conclusions

In summary, Blackberry-like CdS microspheres were synthesized by a facile hydrothermal method. Furthermore, through a simple ion-exchange reaction between the CdS microspheres and $Bi(NO_3)_3 \cdot 5H_2O$, Bi_2S_3 nanorods were uniformly grafted to the surfaces of CdS microspheres and novel urchin-shaped CdS/Bi_2S_3 core/shell heterostructures were successfully fabricated. The content of loading Bi_2S_3 had significantly effects on the photocatalytic activity for the degradation of RhB, and the CdS/Bi_2S_3 heterostructures with the theoretical molar ratio of Bi/Cd (0.25) exhibited the best photocatalytic activity, which is about 2.5 and 9.5 times higher than those of pure CdS and Bi_2S_3, respectively. More interestingly, the CdS/Bi_2S_3 heterostructures exhibit high stabilities under illumination, compared with pure CdS. The enhancement in both photocatalytic performance and stability can be ascribed to the enhancement of visible light absorption and the effective separation and transfer of photogenerated charges originating from the well-matched band-structures and closely contacted heterojunction interfaces. It is expected that the design idea and synthetic methodology could be extended to other heterostructured photocatalysts that might possess potential applications in energy and environmental fields.

Acknowledgements

The authors are grateful for the financial support from the National Science Foundation of China (Grant No. 20871042), the Key Science and Technology Program of Henan Province, PR China (Grant No.122102210232, 122102210233, and 132102210439), the Basic Scientific and Technological Frontier Project of Henan Province, PR China (Grant No.132300410286), Natural Science Foundation of the Education Department of Henan Province (No. 2011A150019 and 2008B430012), and Specialized Research Fund for the Doctoral Program of Higher Education of China (No. 20104104110004).

Figure Captions

Fig.1 XRD patterns of the as-prepared samples: (a) pure CdS, (b) BC-0.1, (c) BC-0.25, (d) BC-0.5, (e) BC-1.0 and (f) pure Bi_2S_3.

Fig.2 XPS spectra of the BC-0.25 sample: (a) survey spectrum, (b) Cd 3d, (c) Bi 4f and (d) S 2s

Fig. 3 SEM images of the as-prepared samples:: (a) pure CdS, (b) BC-0.1, (c) BC-0.25, (d) BC-0.5, (e) BC-1.0 and (f) pure Bi_2S_3.

Fig. 4 TEM images (a), HRTEM image (b) and EDS patterns (c) of the BC-0.25 sample.

Fig. 5 UV-vis diffuse reflectance spectra of the as-prepared samples: (a) pure CdS, (b) BC-0.1, (c) BC-0.25, (d) BC-0.5, (e) BC-1.0 and (f) pure Bi_2S_3

Fig. 6 PL spectra of the pure CdS, Bi_2S_3 and the BC-0.25 samples.

Fig. 7 UV-vis spectral changes of RhB as a function of irradiation time over (a) pure CdS, (b) Bi_2S_3 and (c) the BC-0.25 samples.

Fig. 8 (a) Photodegradation efficiencies (C/C_0) of RhB as a function of irradiation time by different photocatalysts under visible light irradiation; (b) First-order kinetics plot for the photodegradation of RhB.

Fig. 9 Cycling runs for the photocatalytic degradation of RhB in the presence of the BC-0.25 sample (square) and pure CdS (circle).

Fig. 10 XRD patterns of pure CdS and the BC-0.25 sample before and after the photodegradation.

Fig. 11 Diagram for energy band levels of the CdS/Bi_2S_3 heterostructures and the possible charge separation process.

References

1. P. Y. Dong, Y. H. Wang, B. C. Cao, S. Y. Xin, L. N. Guo, J. Zhang and F. H. Li, *Appl. Catal. B: Environ.*, 2013**, 132-133**, 45-53.
2. H. Tong, S. X. Ouyang, Y. P. Bi, N. Umezawa, M. Oshikiri and J. H. Ye, *Adv. Mater.*, 2012**, 24** , 229-251.
3. Y. Wang, S. Li, X. R. Xing, F. Z. Huang, Y. H. Shen, A. J. Xie, X. F. Wang and J. Zhang, *Chem. Eur. J.*, 2011**, 17**, 4802-4808.
4. H. Katsumata, M. Taniguchi, S. Kaneco and T. Suzuki, *Catal. Commun.*, 2013**, 34,** 30-34.
5. X. Li, J. Zhu and H. X. Li, *Appl. Catal. B: Environ.*, 2012, **123-124**, 174-181.
6. I. J. Plante, A. Teitelboim, I. Pinkas, D. Oron and T. Mokari, *J. Phys. Chem. Lett.*, 2014, **5**, 590-596.
7. Y. D. Liu, L. Ren, X. Qi, Y. Wang, X. J. Liu and J. X. Zhong, *RSC Adv.*, 2014, **4**, 8772-8778.
8. C. Z. Wei, C. Cheng, J. H. Zhao, S. S. Zheng, M. M. Hao and H. Pang, *Dalton Trans.*, 2014, **43**, 5687-5693.
9. Y. Q. Shi, K. Q. Zhou, B. B. Wang, S. H. Jiang, X. D. Qian, Z. Gui, R. K. K. Yuen and Y. Hu, *J.Mater. Chem. A*, 2014, **2**, 535-544.
10. G. P. Chen, D. G. Li, F. Li, Y. Z. Fan, H. F. Zhao, Y. H. Luo, R. C. Yu and Q.B. Meng, *Appl. Catal. A: Gen.*, 2012, **443-444**, 138-144.
11. J. H. Yang, H. J. Yan, X. L. Wang, F. Y. Wen, Z. J. Wang, D. Y. Fan, J. Y. Shi and C. Li, *J. Catal.*, 2012, **290**, 151-157.
12. F. Jiang, T. T. Yan, H. Chen, A.W. Sun, C. M. Xu and X. Wang, *Appl. Surf. Sci.*, 2014, **295**, 164-172.
13. Z. Y. Wu, G. H. Zhao, Y. N. Zhang, H.Y. Tian and D.M. Li, *J. Phys. Chem. C*, 2012, **116**, 12829-12835.
14. L. H. Lai, L. Protesescu, M. V. Kovalenko and M. A. Loi, *Phys. Chem. Chem. Phys.*, 2014, **16**, 736-742.
15. M. M. Liu, J. T. Zheng, Q. Liu, S. J. Xu, M. B. Wu, Q. Z. Xue, Z. F. Yan, H. J. Xiao, Z. X. Wei and H. Y. Zhu, *RSC Adv.*, 2013, **3**, 9483-9489.
16. A. Kar, S. Kundu and A. Patra, *RSC Adv.*, 2012, **2**, 10222-10230.
17. A. Hernández-Gordillo, A. G. Romero, F. Tzompantzi and R. Gómez, *Appl. Catal. B: Environ.*, 2014, **144**, 507-513.
18. X. X. Zhou, H. R. Chen, Y. Y. Sun, K. Zhang, X. Q. Fan, Y. Zhu, Y. Chen, G. J. Tao and J. L. Shi, *Appl. Catal. B: Environ.*, 2014, **152-153**, 271-279.
19. H. Zhang and Y. F. Zhu, *J. Phys. Chem. C*, 2010, **114**, 5822-5826.
20. J. Y. Zhang, Y. B. Wang, J. Jin, J. Zhang, Z. Lin, F. Huang and J. G. Yu, *ACS Appl. Mater. Interfaces*, 2013, **5**, 10317-10324.
21. J. Fu, B. B. Chang, Y. L. Tian, F. N. Xi and X. P. Dong, *J. Mater. Chem. A*, 2013, **1**, 3083-3090.
22. T. Wu, X. G. Zhou, H. Zhang and X. H. Zhong, *Nano Res.*, 2010, **3**, 379-386.
23. L. S. Li, R. G. Cao. Z. J. Wang, J. J. Li and L. M. Qi, *J. Phys. Chem. C*, 2009, **113**, 18075-18081.
24. J. Cao, B. Y. Xu, H. L. Lin, B. D. Luo and S. F. Chen, *Catal. Commun.*, 2012, **26**, 204-208.

25. S. Balachandran and M. Swaminathan, *Dalton Trans.*, 2013, **42**, 5338-5347.
26. S. R. Luo, F. Chai, L. Y. Zhang, C. G. Wang, L. Li, X. C. Liu and Z. M. Su, *J. Mater. Chem.*, 2012, **22** , 4832-4836.
27. N. Liang, J. T. Zai, M. Xu, Q. Zhu, X. Wei and X. F. Qian, *J. Mater. Chem. A*, 2014, **2**, 4208-4216.
28. A. Jana, C. Bhattacharya and J. Datta, *Electrochimica Acta,*2010, **55**, 6553-6562.
29. S. S. D. Mishra, K. K. Saini, C. Kant, and M. Pal, *Mater. Chem. Phys.*2014, **146**, 324-329.
30. X. Li, J. Chen, H. Li, J. Li, Y. Xu, Y. Liu and J. Zhou, *J. Nat. Gas Chem.* 2011, **20**, 413-417.
31. Z. Fang, Y. F. Liu, Y. T. Fan, Y. H. Ni, X. W. Wei, K. B. Tang, J. M. Shen and Y. Chen, *J. Phys. Chem. C*, 2011, **115**, 13968-13976.
32. X. B. He, L. Gao, S. W. Yang and J. Sun, *CrystEngComm*, 2010, **12**, 3413-3418.
33. C. Wang, Y. H. Ao, P. F. Wang, J. Hou, J. Qian and S. H. Zhang, *Mater. Lett.*, 2010, **64**, 439-441.
34. G. Q. Tan, L. L. Zhang, H. J. Ren, S. S. Wei, J. Huang and A. Xia, *ACS Appl. Mater. Interfaces*, 2013, **5**, 5186-5193.
35. G. R. Yang, W. Yan, Q. Zhang, S. H. Shen and S. J. Ding, *Nanoscale*, 2013, **5**, 12432-12439.
36. J. Cao, B.Y. Xu, H. L. Lin, B. D. Luo and S. F. Chen, *Dalton Trans.*, 2012, **41**, 11482-11490.
37. H. N. Kim, T. W. Kim, K.-H. Choi, I. Y. Kim, Y.-R. Kim and S.-J. Hwang, *Chem. Eur. J.*, 2011, **17**, 9626-9633.
38. X. Li, C. Hu, X. Wang and Y. Xi, *Appl. Surf. Sci.*, 2012, **258**, 4370-4376.
39. L. Huang, J. H. Yang, X. L. Wang, J. F. Han, H. X. Han and C. Li, *Phys. Chem. Chem. Phys.*, 2013, **15**, 553-560.
40. M. L. Guan, D. K.Ma, S. W. Hu, Y. J. Chen and S. M. Huang, *Inorg. Chem.,* 2011, **50**, 800-805.
41. D. Sarkar, C. K. Ghosh, S. Mukherjee and K. K. Chattopadhyay, *ACS Appl. Mater. Interfaces,* 2013, **5**, 331-337.
42. M. Y. Liu, L.Q. Zhang, X. X. He, B. Zhang, H. F. Song, S. N. Li and W. S. You, *J. Mater. Chem. A*, 2014, **2**, 4619-4626.
43. Z. D. Wu, L. L. Chen, C. S. Xing, D. L. Jiang, J. M. Xie and M. Chen, *Dalton Trans.*, 2013, **42**, 12980-12988.
44. J. H. Chen, S. Y. Qin, G. X. Song, T. Y. Xiang, F. Xin and X. H. Yin, *Dalton Trans.*, 2013, **42**, 15133-15138.
45. J. Cao, B. Y. Xu, B. D. Luo, H. L. Lin and S. F. Chen, *Catal. Commun.*, 2011, **13**, 63-68.
46. L. Huang, X. L.Wang, J. H. Yang, G. Liu, J. F. Han and C. Li, *J. Phys. Chem. C*, 2013, **117**, 11584-11591.
47. Y. Liu, Y.-X. Yu and W.-D. Zhang, *J. Phys. Chem. C*, 2013, **117**, 12949-12957.
48. Y. L. Min, G. Q. He, Q. J. Xu and Y. C. Chen, *J. Mater. Chem. A*, 2014, **2**, 2578-2584.

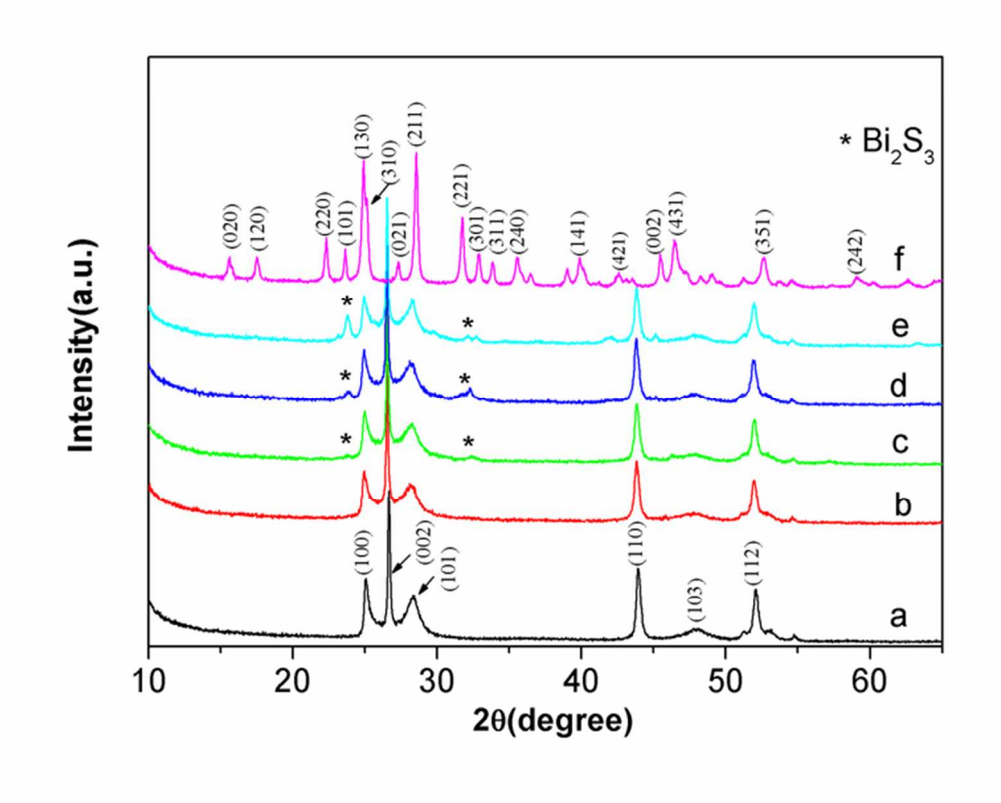

Fig.1 XRD patterns of the as-prepared samples: (a) pure CdS, (b) BC-0.1, (c) BC-0.25, (d) BC-0.5, (e) BC-1.0 and (f) pure Bi2S3.
64x51mm (300 x 300 DPI)

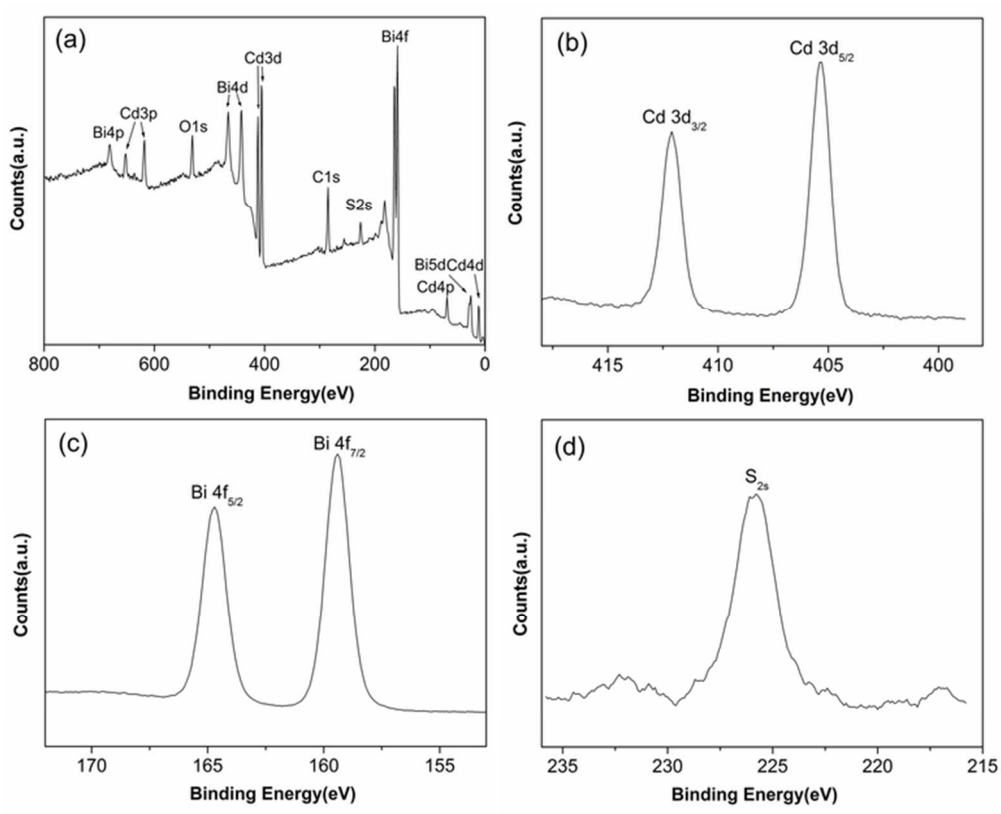

Fig.2 XPS spectra of the BC-0.25 sample: (a) survey spectrum, (b) Cd 3d, (c) Bi 4f and (d) S 2s
65x53mm (300 x 300 DPI)

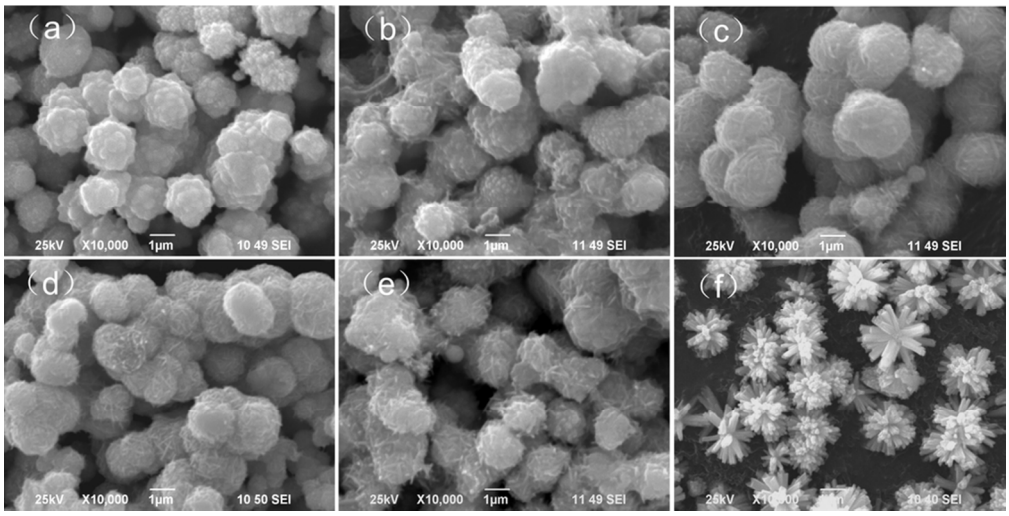

Fig. 3 SEM images of the as-prepared samples:: (a) pure CdS, (b) BC-0.1, (c) BC-0.25, (d) BC-0.5, (e) BC-1.0 and (f) pure Bi2S3.
85x43mm (300 x 300 DPI)

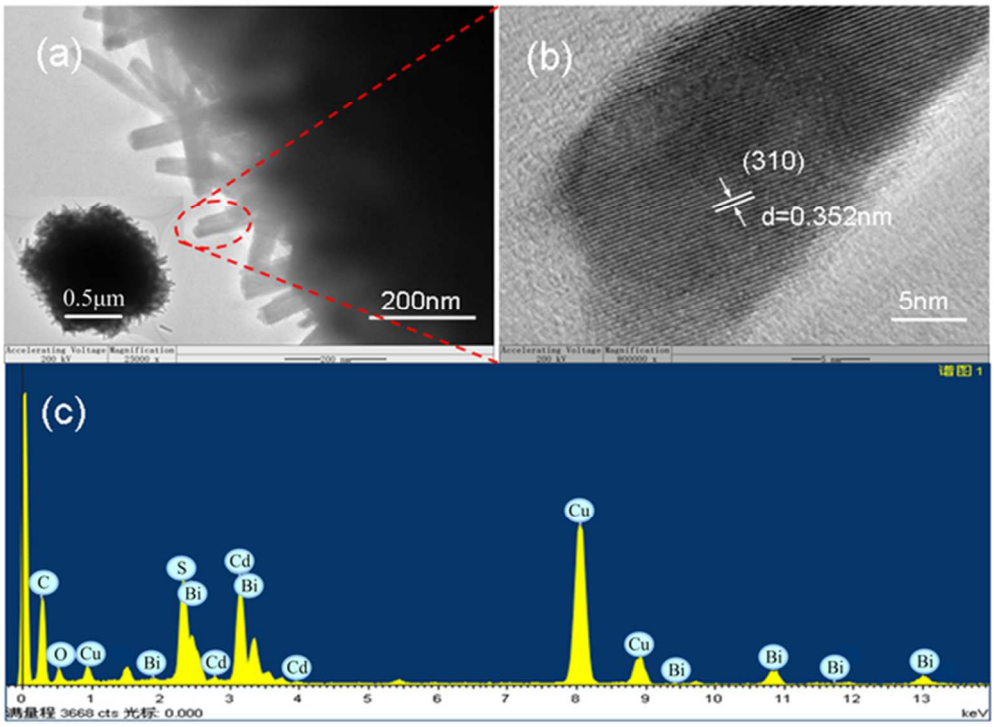

Fig. 4 TEM images (a), HRTEM image (b) and EDS patterns (c) of the BC-0.25 sample.
57x42mm (300 x 300 DPI)

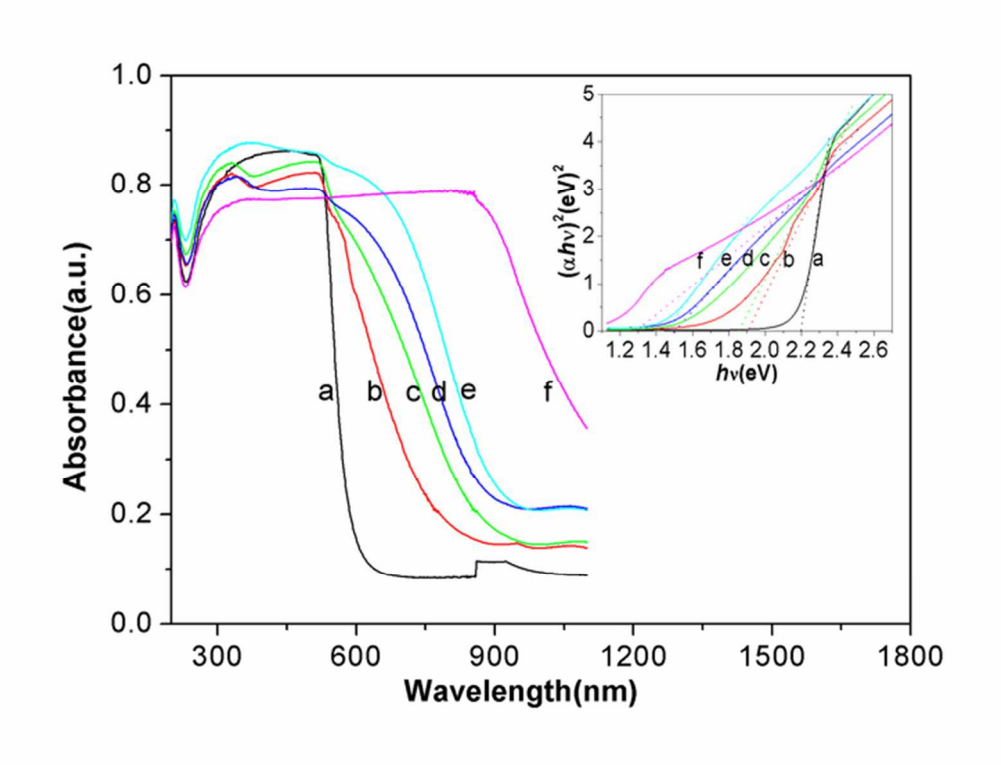

Fig. 5 UV-vis diffuse reflectance spectra of the as-prepared samples: (a) pure CdS, (b) BC-0.1, (c) BC-0.25, (d) BC-0.5, (e) BC-1.0 and (f) pure Bi2S3
61x46mm (300 x 300 DPI)

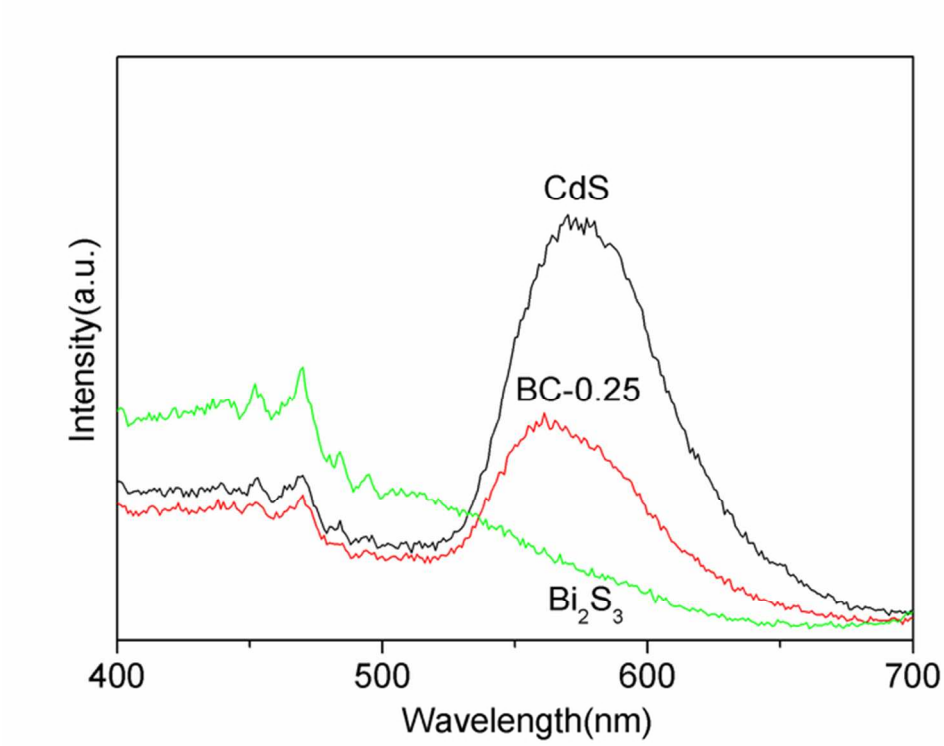

Fig. 6 PL spectra of the pure CdS, Bi2S3 and the BC-0.25 samples.
64x51mm (300 x 300 DPI)

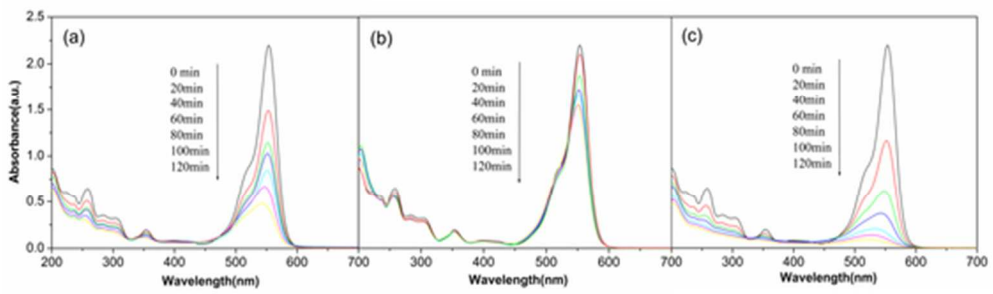

Fig. 7 UV-vis spectral changes of RhB as a function of irradiation time over (a) pure CdS, (b) Bi2S3 and (c) the BC-0.25 samples.
48x14mm (300 x 300 DPI)

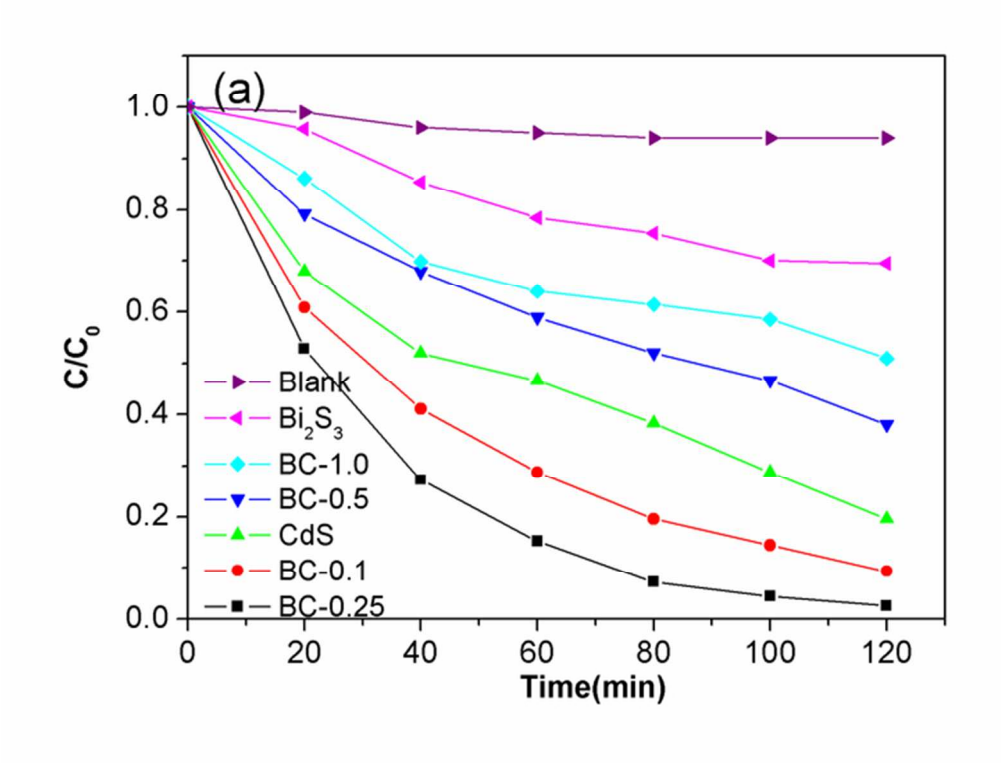

Fig.8(a) Photodegradation efficiencies (C/C0) of RhB as a function of irradiation time by different photocatalysts under visible light irradiation;
61x46mm (300 x 300 DPI)

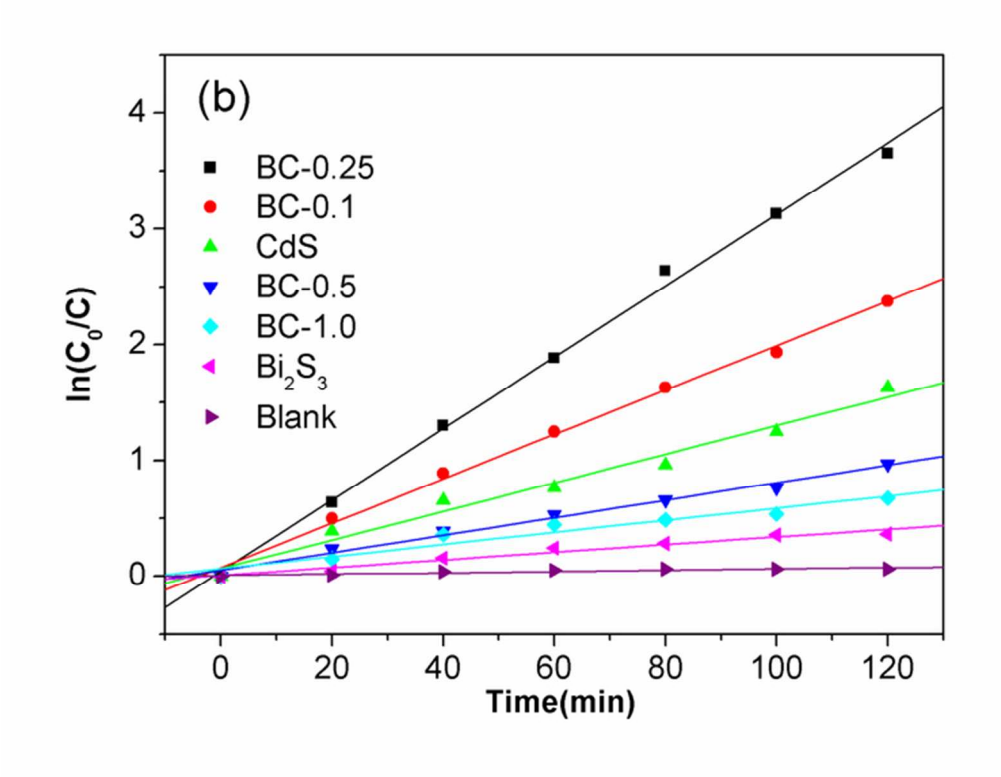

Fig.8(b) First-order kinetics plot for the photodegradation of RhB.
62x48mm (300 x 300 DPI)

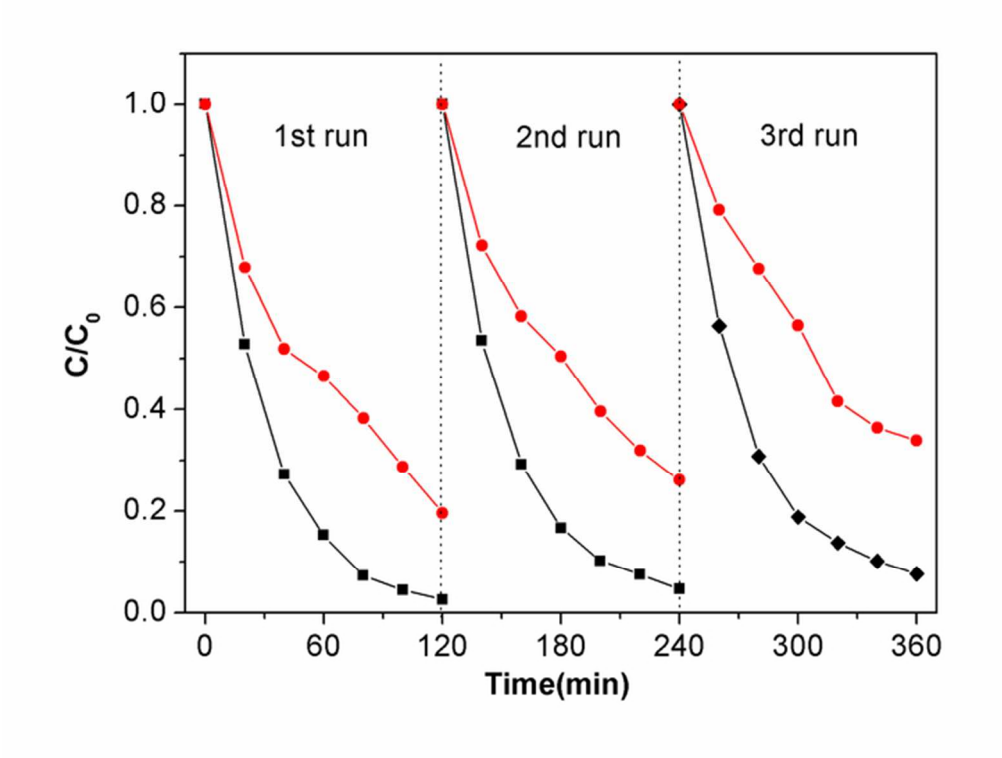

Fig.9 Cycling runs for the photocatalytic degradation of RhB in the presence of the BC-0.25 sample (square) and pure CdS (circle).
60x46mm (300 x 300 DPI)

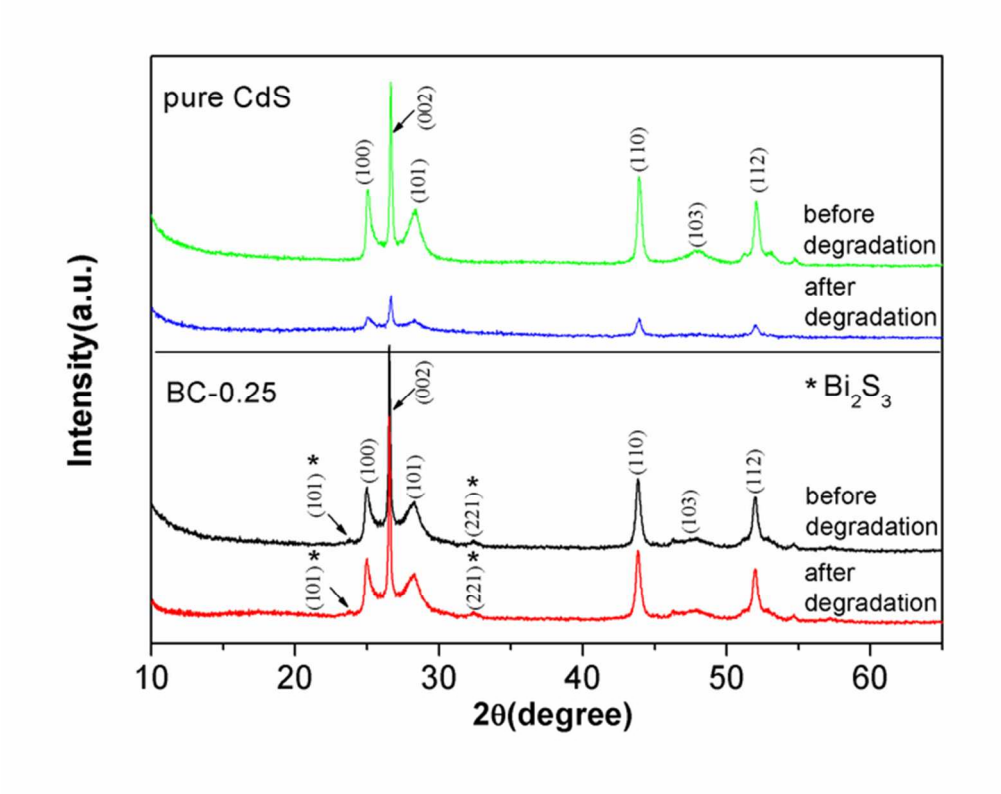

Fig. 10 XRD patterns of pure CdS and the BC-0.25 sample before and after the photodegradation.
63x50mm (300 x 300 DPI)

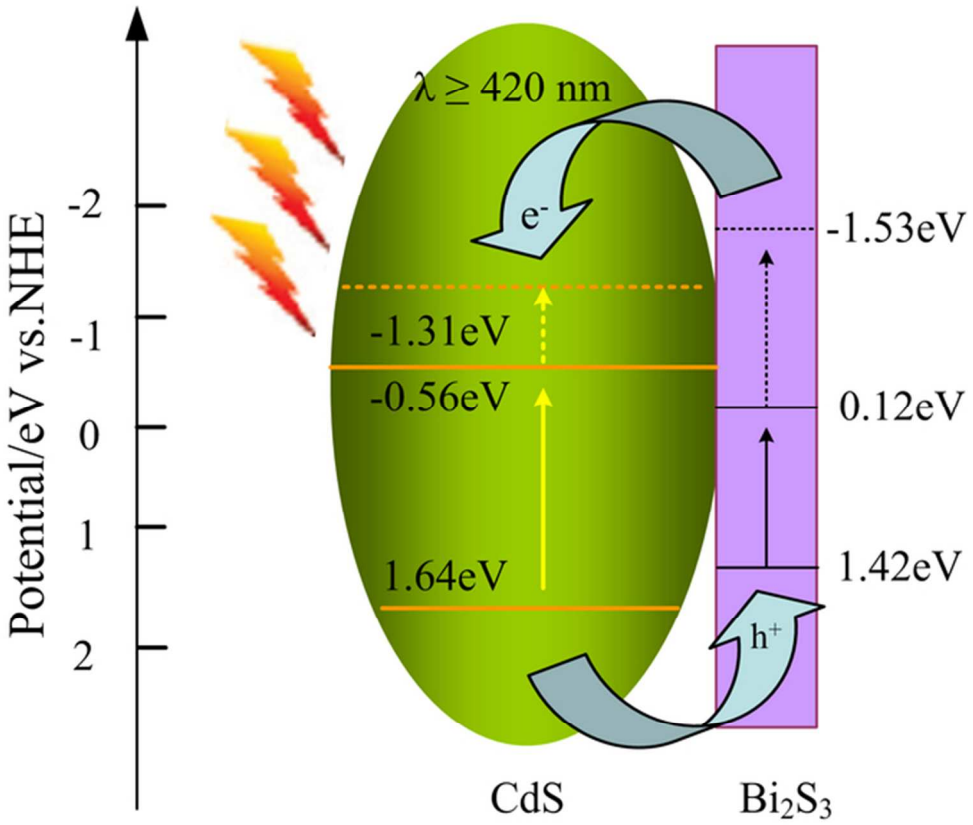

Fig. 11 Diagram for energy band levels of the CdS/Bi2S3 heterostructures and the possible charge separation process.
59x49mm (300 x 300 DPI)